Growing oxide thin films in a low-energy electron microscope

Torren, A.J.H. van der

7

Growing a $LaAlO_3/SrTiO_3$ heterostructure on $Ca_2Nb_3O_{10}$ nanosheets

The two-dimensional electron gas between the band insulators $LaAlO_3$ and $SrTiO_3$ is a promising component for oxide eletronics, but the requirement of single crystal substrates for the growth limits its applications. It is therefore important to find ways to deposit these materials on other substrates. Interesting candidates are nanosheets of $Ca_2Nb_3O_{10}$ which can be used as seed layers for perovskite materials on any substrate. These nanosheets can reach a lateral size of several microns. Low-energy electron microscopy with in-situ *pulsed laser deposition allows us to study the growth on these flakes as well as to fingerprint the electronic properties. We grow a $LaAlO_3/SrTiO_3$ heterostructure on $Ca_2Nb_3O_{10}$ nanosheets deposited on a Si substrate and find that it shows the fingerprints of a two-dimensional electron gas.*

This chapter will be submitted as:

A.J.H. van der Torren, H. Yuan, J. Jobst, J.E. ten Elshof, M. Huijben, A.J.H.M. Rijnders, G. Koster, S.J. van der Molen, J. Aarts, *Growing a $LaAlO_3/SrTiO_3$ heterostructure on $Ca_2Nb_3O_{10}$ nanosheets*

7.1 Introduction

Transition metal oxides (TMO's) and especially the group with the perovskite crystal structure is an interesting group of materials with a great varity of physical properties. Moreover, stacking layers of different metal oxides allows for new properties to be made on design. A well known example is the formation of the two-dimensional electron gas (2-DEG) between $SrTiO_3$ and $LaAlO_3$ [1].

Typically, these materials are grown on single crystals, which is impractical for industrial applications. This limitation can be overcome by growing $SrTiO_3$ on a simpler substrate. Growth on Si is possible [2], but here we use a different approach and use inorganic nanosheets. Such sheets can be obtained through exfoliation of materials which allow a close match with the lattice parameter of the deposited $SrTiO_3$ layer. In our case that is $Ca_2Nb_3O_{10}$ on which the growth of epitaxial $SrTiO_3$, $SrRuO_3$ and $BiFeO_3$ has already been shown [3]. This nanosheet approach is very flexible, as nanosheets can be deposited on virtually any substrate [3–6], rendering design freedom in tailoring device properties.

Compared to the conventional case where the $LaAlO_3/SrTiO_3$ 2-DEG resides on top of half a millimeter thick $SrTiO_3$ substrate, the exfoliated nanosheets have a thickness of only 1.5 to 4 nm [6–9]. This allows to dramatically reduce the thickness of the $SrTiO_3$ dielectric, which is particularly useful if that is to be used as a backgate.

To make optimal use of this advantage, it is important to understand the formation of the 2-DEG in the limit of a minimal thickness of the $LaAlO_3/SrTiO_3$ grown on the nanosheets. Low-energy electron microscopy (LEEM) with *in-situ* pulsed laser deposition (PLD) is the ideal tool to study the growth and electronic properties of these heterostructures in a laterally resolved manner [10]; as already discussed in chapter 5.

In this chapter we show the growth of $LaAlO_3/SrTiO_3$ heterostructures on $Ca_2Nb_3O_{10}$ nanosheets which have been deposited on a Si substrate. We use a combined LEEM/PLD system to study the details of the growth in real time and to investigate the electronic structure of the material we grow. We compare the results obtained on nanosheets with conventional $LaAlO_3/SrTiO_3$ heterostructures on a $SrTiO_3$ substrate to judge the quality of the heterostructure.

7.2 Experimental

$Ca_2Nb_3O_{10}$ nanosheets where synthesized and deposited by Langmuir-Blodgett (LB) deposition on insulating Si substrates as described elsewhere [6]. The samples were first transferred into the ESCHER LEEM system [10–13] with *in-situ* pulsed laser deposition as described in chapter 5. Before starting the growth, they were annealed at 570 °C (measured with a pyrometer using an emissivity of 0.7) for at least half an hour in an oxygen background pressure of 5×10^{-5} mbar, in order to remove any contaminants.

A home-built PLD system was used to grow the materials *in-situ*. In fact, PLD growth and LEEM imaging is performed in an alternating fashion: the high voltage

between objective lens and sample, which is required to decelerate the low-energy electrons for imaging, is turned off during the deposition performed by 5 to 10 laser pulses, depending on the material growth speed. After that the high voltage is quickly ramped up again to image the sample. These cycles of roughly 3 min each are repeated until a film of the desired thickness is grown. During the process, temperature and pressure are kept constant.

For the deposition of $SrTiO_3$ onto the nanosheets, the temperature was raised to 660 °C. PLD was performed with a laser fluence of $1.4\,J/cm^2$ and a 1 Hz repetition rate in 5×10^{-5} mbar oxygen. In chapter 5 it was discussed that these parameters for the growth of $SrTiO_3$ can result in slightly off-stoichiometric growth. However, it was not possible to further optimize the growth at the low pressures our microscope is limited to. Following the deposition, the sample was annealed at 770 °C for at least half an hour in the same oxygen pressure, in order to improve the surface flatness. The sample was then cooled down and moved to the transfer chamber (2×10^{-9} mbar) while the $SrTiO_3$-target was replaced with a $LaAlO_3$-target. After a pre-ablation step of the $LaAlO_3$-target, the sample was transferred back to the measurement position. It was heated to 750 °C at the same oxygen pressure of 5×10^{-5} mbar. $LaAlO_3$ was then deposited at a laser fluence of $2.0\,J/cm^2$ and 1 Hz repetition rate. In chapter 6 it was shown that these parameters result in a conducting $LaAlO_3/SrTiO_3$ interface. Three samples were made, called A to C, with $SrTiO_3$ thicknesses estimated to be 3.4 nm, 5.6 nm and 5.5 nm, respectively. For comparison, $LaAlO_3$ was grown on a TiO_2-terminated[14] $SrTiO_3$-substrate under the same growth conditions (sample D).

The nanosheet starting material, the whole growth process and the final heterostructures were investigated by various techniques available in the LEEM. LEEM provides real-space images while low-energy electron diffraction (LEED) is used to study the crystal structure. The ability to quickly switch between real-space imaging and diffraction in combination with µLEED (confining the probing electron beam to sub-micron size by putting an aperture in the beam path) allows for investigation of the crystal structure of the independent flakes. LEEM-IV spectra or IV-curves (the intensity of reflected electrons as a function of their landing energy) yield clear fingerprints of the different surface layers[15]. Angle-resolved reflected-electron spectroscopy (ARRES)[16] extends the concept of IV-curves by recording electron reflectivity maps as a function of landing energy and in-plane wave vector $k_{\parallel}$ of the electrons. Such ARRES maps are correlated with the unoccupied band structure of the surface layer and are therefore well suited to probe the surface stoichiometry of the $LaAlO_3$-layer. This implicitly indicates whether or not a 2-DEG is formed at the $LaAlO_3/SrTiO_3$ interface as was shown in chapter 6.

7.3 Results

Figure 7.1a shows a LEEM image of $Ca_2Nb_3O_{10}$ nanosheets deposited on Si (sample A). Individual nanosheets can clearly be recognized, of which the sheet covering the bottom half of the image is the biggest. In the top half, four medium size flakes

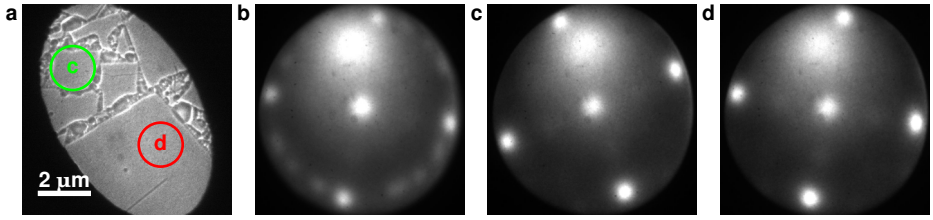

FIGURE 7.1: a) LEEM image of nanosheets on Si (sample A) with circles in red (lower right) and green (upper left) around the areas where images c and d are taken. b) Diffraction pattern taken on sample A. Note that apart from the four strong reflections there are numerous weak ones on the circle in between them. c) µLEED image of area indicated with the green circle (upper, left) in (b). d) µLEED pattern of area indicated with the red circle (lower, right). All diffraction patterns are taken at 14 eV landing energy. The real-space image is taken close to 0 eV landing energy.

can be recognized with some smaller ones in between. The square surface net expected for $Ca_2Nb_3O_{10}$ is visible in the LEED image (Fig. 7.1b) taken on the same area as fig. 7.1a. Besides the bright four spots originating from the big flake covering the bottom half of the image, many other rotated patterns are visible originating from the flakes in the top half of the image. This indicates that the individual nanosheets are rotated with respect to one another. The rotations of the individual flakes can be determined by taking µLEED images. Figure 7.1c,d show such µLEED patterns of the areas indicated with green (left, top) and red (right, bottom) circles in the LEEM image in Fig. 7.1a. Note that the diffraction spots are not very sharp. This could be caused by imperfect crystallinity of the nanosheets or absorbates at the surface[17].

After characterizing the starting material, we grew $SrTiO_3$ on the sheets by PLD. For the growth, the temperature was raised to 660 °C. Higher temperatures showed degradation of the diffraction pattern. Figure 7.2a and b show the evolution of the intensity and full-width-half-maximum (FWHM) of the specular (0,0) diffraction spot during the growth process for the whole range of energies between 0 and 25 eV. Basically, figure 7.2a shows a series of IV-curves for the specular beam. This reflected intensity is related to the unoccupied band structure (see discussion below) and therefore is a fingerprint of the material studied. During growth we observe a clear change of the IV-curves (vertical cuts through Fig. 7.2a) and therefore a change in the electronic fingerprint of the surface. The IV-curves converge to a constant spectrum around 300 pulses which consists of maxima around 3, 8 and 15 eV. A typical single IV-curve out of this collection will be given and discussed below.

The FWHM of the specular (0,0) diffraction spot (Fig. 7.2b) is sensitive to the crystallinity of the material as well as to the surface roughness. While a small coherence length in the crystal structure broadens the FWHM over all the energies,

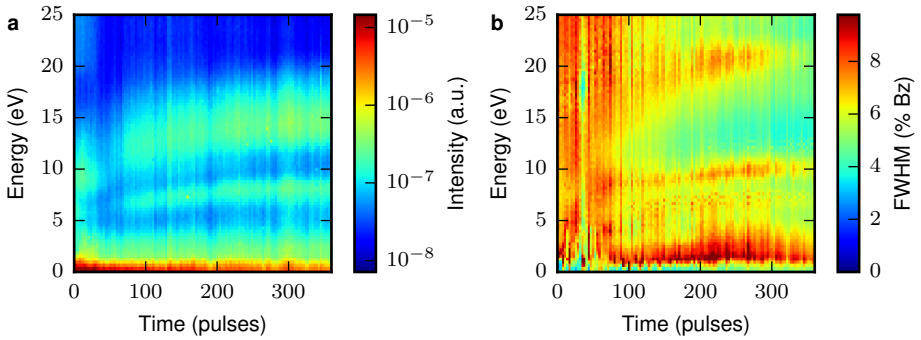

FIGURE 7.2: intensity (a) and FWHM (b) map of the specular (0,0) diffraction spot versus energy during deposition of $SrTiO_3$ on sample A. The intensity map shows a clear change in material, while the FHWM maps shows sharpening of the diffraction spots. Moreover the FWHM becomes energy dependent. The FWHM is given in percentage of the Brillouin zone size.

the surface roughness only influences the FWHM at energies where the incoming and reflected electrons destructively interfere along the out-of-plane axis of the crystal[17]. During growth, the diffraction spots became sharper, quantified by a global reduction of the FWHM (Fig. 7.2b). Moreover, the FWHM became energy-dependent. In other words, the crystallinity improved, but the surface was still rough.

Important, however, is that neither the intensity nor the FWHM showed oscillations during growth. Normally, in layer-by-layer growth of these perovskites a completed and flat layer shows high intensity and small FWHM, while a half-completed and rough layer shows a low intensity and large FWHM. This was demonstrated in chapters 5 and 6 for the growth of $SrTiO_3$ and $LaAlO_3$ on $SrTiO_3$. With respect to the intensity it is the same phenomena as is seen in reflection high energy electron diffraction (RHEED).

Such oscillations can hence be used to count the number of layers but, as noted, they were not visible. Instead, both intensity and FWHM are constant, and the FWHM is large. It is not clear whether that is caused by a small coherence length in the material or a non layer-by-layer growth mode with a constant rough surface. Comparing the growth conditions and amount of pulses to earlier measurements in chapter 6, we can however estimate a film thickness close to 9 unit cells. With this estimation the minimal thickness of 300 pulses is equal to about 7 unit cells.

Figure 7.3a shows a section of the specular (0,0) diffraction spot for the original nanosheets (blue, dashed) and nanosheets with $SrTiO_3$ (green, solid) taken at 17 eV. To compare their FWHM, both curves have been normalized, since the intensity on the nanosheets is 8 times smaller than on the $SrTiO_3$/nanosheet heterostructure. The FWHM has been reduced by about a factor two in growing $SrTiO_3$, indicating a factor 2 increase in the coherent size of the lattice. The in-

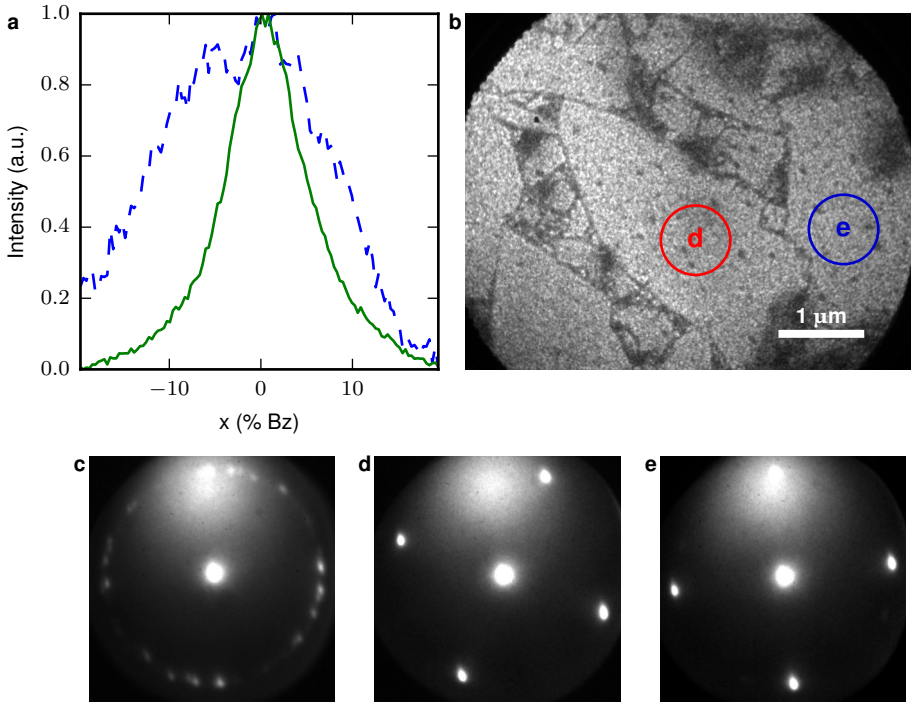

FIGURE 7.3: a) Normalized section of the specular (0,0) diffraction spot on nanosheets (blue, dashed) and after growth of $SrTiO_3$ (green, solid) on sample A taken at 17 eV. The intensity of the blue curves was 1/8 of that of the green curve. b) Bright field image at 29.6 eV with locations of µLEED images d and e indicated in red (left) and blue (right). c) LEED image of the area shown in b. d, e) µLEED image of areas indicated in b. All LEED/µLEED images were taken at 17 eV landing energy.

dividual nanosheets are still clearly visible in the bright field image (Fig. 7.3b), indicating that the STO only grew epitaxially on the sheets. Indeed, the black areas separating individual nanosheets did not show a diffraction pattern, i.e. the material there was not crystalline. Just as on the bare nanosheets, the LEED pattern in Fig.7.3c shows multiple diffraction patterns, while µLEED patterns in Fig. 7.3d and e show single orientations for every $SrTiO_3$/nanosheet heterostructure. These µLEED patterns were taken on the areas indicated with circles in red (left) and blue (right) in Fig. 7.2b, respectively. This suggests the $SrTiO_3$ follows the crystal structure of the underlying nanosheets.

Although the grown $SrTiO_3$ layer was crystalline after deposition, the FWHM of the specular spot was still broad compared to measurements on a single crystal $SrTiO_3$ substrate. To further improve the surface quality we annealed the sample with the following procedure: the sample was slowly heated from 660 °C to 770 °C

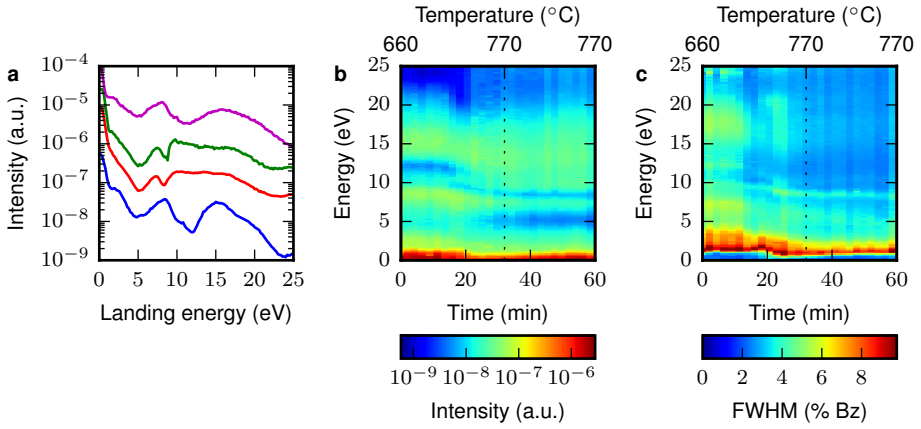

FIGURE 7.4: a) IV-curve before (blue, bottom) and after (red, 2nd from bottom) annealing. As comparison, two IV-curves on a $SrTiO_3$-substrate are shown, TiO_2-terminated (green, 2nd from top) and SrO-terminated (magenta, top). Curves are shifted for clarity. Intensity (b) and FWHM (c) versus energy during the annealing process on sample B. Over the first half an hour the temperature was slowly increased from 660 °C to 770 °C and was kept constant for the next half an hour. The dotted line separates the time the temperature was ramped and the time it was kept constant. The FWHM is given in percentage of Brillouin zone.

in 30 min and was held there for another 30 min. During the annealing the oxygen pressure was 5×10^{-5} mbar, equal to the pressure used during PLD. The maximum of 770 °C was the maximum temperature for which the diffraction pattern does not start to degrade.

The annealing not only changes the surface roughness but also the surface electronic properties. This is demonstrated in figure 7.4 taken on sample B ($SrTiO_3$ thickness of about 5.6 nm, i.e. 600 PLD pulses). Figure 7.4a shows four IV-curves, from bottom to top: sample B before annealing (blue), sample B after annealing (red), a reference curve taken on a TiO_2-terminated $SrTiO_3$-substrate (green) and a curve taken on a SrO-terminated $SrTiO_3$-substrate (magenta). The reference curves were taken from chapter 6 where the $SrTiO_3$ was TiO_2-terminated by HF-etching[14] and the SrO-termination was obtained by the growth of an SrO bilayer on a TiO_2-terminated substrate. From the IV-curves before and after annealing we can conclude the surface changes from a dominantly SrO-termination to a TiO_2-termination.

The material evolution is shown in more detail in figure 7.4b, which shows the IV-curve change over time during annealing, and figure 7.4c which shows the corresponding change of the FWHM. The FWHM further decreased and the energy dependence disappeared, i.e. the surface flattened. From the FWHM and intensity together we conclude that the change of the material and the flattening of the surface go hand in hand.

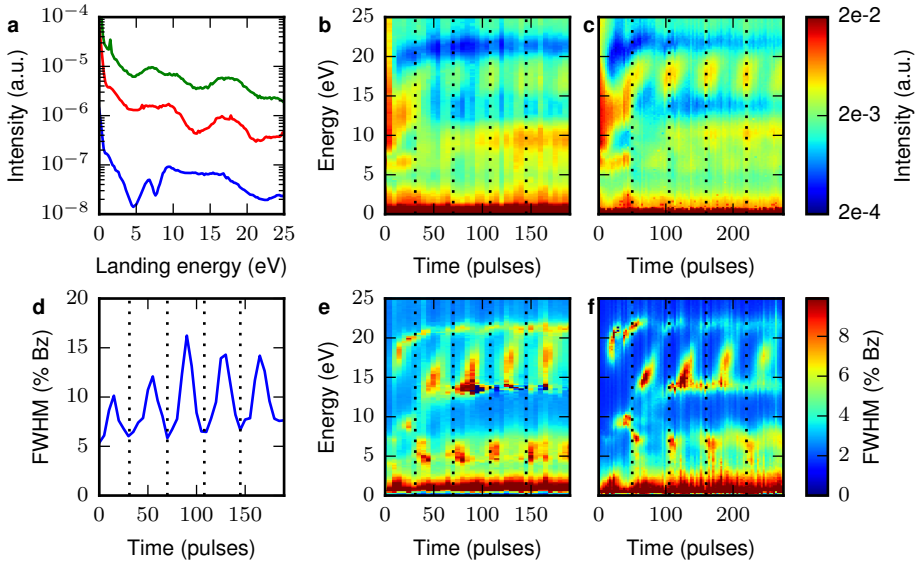

FIGURE 7.5: a) IV-curve before (blue, bottom) and after (red, middle) growth of $LaAlO_3$ on sample C. Furthermore, a reference curve of 5 unit cells $LaAlO_3$ on a $SrTiO_3$ substrate on sample D̃ (green, top) is shown. b) Intensity map versus time and energy of the specular (0,0) diffraction spot on sample C. c) the same map on reference sample D. d) FWHM oscillations versus time at 16 eV, on sample C. This energy is close to the out-of-phase conditions where maximal surface sensitivity is reached. e) FWHM map for all energies on sample C and f) FWHM map on sample D.

After improving the $SrTiO_3$ surface in this way and confirming it is TiO_2-terminated, a thin film of $LaAlO_3$ was grown. Figure 7.5a shows the IV-curves before (blue, bottom) and after (red, middle) growth on sample C ($SrTiO_3$ thickness of about 5.5 nm, i.e. 588 PLD pulses). Furthermore, a reference curve of 5 unit cells $LaAlO_3$ grown under the same conditions on a $SrTiO_3$-substrate (sample D) (green, top) is shown. The IV-curves after growth on the nanosheets and on the $SrTiO_3$-substrate are very similar, confirming that the same quality $LaAlO_3$ was grown in both cases. The evolution of the IV-curves during growth is shown in figure 7.5b for sample C and in figure 7.5c for the reference sample D. The same structure is found for both samples, i.e. they show the same type of growth. Both samples show oscillations in intensity around 16 eV, indicating layer-by-layer growth. As a guide to the eye, vertical dotted lines indicate the full unit cells. These growth oscillations are more clear from the FWHM at 16 eV, which is plotted for the nanosheet sample in figure 7.5d. This energy is close to the interference condition with the out-of-plane crystal axis. The FWHM for all energies from 0 to 25 eV is shown in figure 7.5e and f for the nanosheet sample C and the reference sample D. Here again we observe the same growth pattern for $LaAlO_3$ grown on the $SrTiO_3$/nanosheet heterostructure

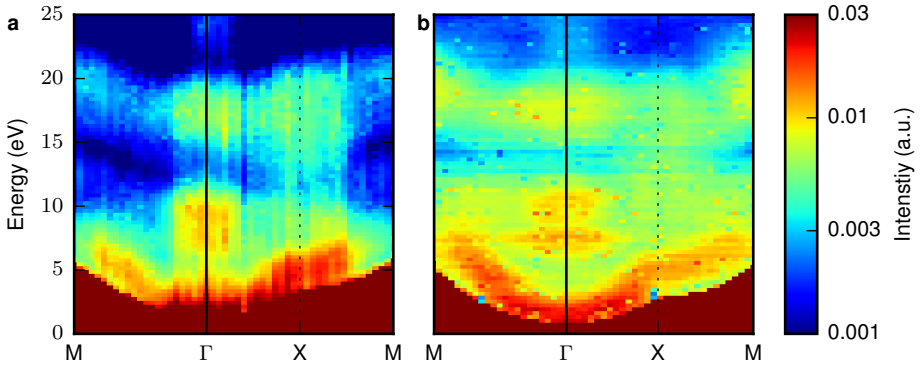

FIGURE 7.6: a) ARRES map of $LaAlO_3/SrTiO_3$ on $Ca_2Nb_3O_{10}$ nanosheets (sample C) and b) ARRES map of $LaAlO_3$ on $SrTiO_3$ substrate (sample D). On both samples 5 unit cells of $LaAlO_3$ have been grown. Both images are on the same energy scale.

and on a TiO_2-terminated $SrTiO_3$-substrate. Comparing the IV-curves to earlier measurements on conducting and non-conducting samples in chapter 6 suggests that the interface between the $LaAlO_3$ and $SrTiO_3$ should show conductivity.

The possible presence of a 2-DEG at the $LaAlO_3/SrTiO_3$ interface can be probed in more detail by comparing ARRES[16] measurements of the $LaAlO_3/SrTiO_3$/nanosheets heterostructure (Fig. 7.6a, sample C) and the reference sample D of $LaAlO_3$ on a TiO_2-terminated $SrTiO_3$-substrate (Fig. 7.6b).

ARRES is, as explained earlier, an extension of the IV-curve by recording electron reflectivity maps as a function of landing energy and in-plane wave vector $k_{\|}$ of the electrons, forming a kind of band structure map of the unoccupied bands above the vacuum energy. Both of the ARRES maps show similar features. Most pronounced is the band gap just above the mirror mode energy, the lowest energy when the electrons just touch the sample, for all $k_{\|}$. Furthermore, pronounced features can be found at energies between 7 and 10 eV and around 17 eV both around the Γ-point. Band gaps are presented in ARRES as maxima because the probing low-energy electrons are reflected with high probability if no states exist in the material at that energy (E) and in-plane wave vector ($k_{\|}$). The dispersion of band gaps and bands was also similar for both samples, e.g. the band gap around 17 eV extends parabolically to the M-point around 20 eV and the band gaps around the X-point at 10 and 17 eV connect.

The differences between the two maps can partially be explained by the different data acquisition methods used. For reference sample D, data is obtained from diffraction patterns, averaging a 20 μm^2 area. On the other hand, for the nanosheet sample C, data from a 20 μm^2 area would average the signal of multiple flakes. Due to the random orientation of the flakes, the in-plane wave vector of the electrons would be badly defined in the crystal bases. This can be solved by taking real-space

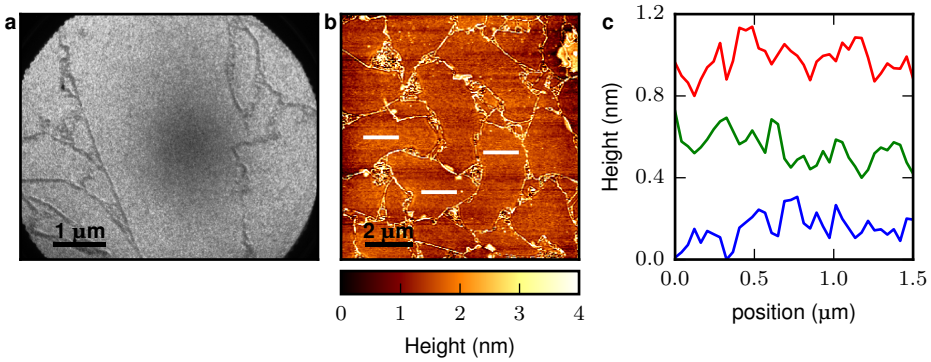

FIGURE 7.7: a) Bright field image at 16 eV and b) AFM image of the $LaAlO_3/SrTiO_3/Ca_2Nb_3O_{10}$ heterostructure (sample C). c) Line profiles of the relative height difference on the nanosheets, profiles from bottom to top correspond to white lines in (b) from left to right. The dark area in the center of image (a) is due to an inhomogeneous channel plate.

data, where the signal of a single flake can be selected in the post processing [16]. In order to take real-space images the specular diffraction spot has to be selected by an aperture during acquisition. Due to the finite size of the aperture, an average is taken over the specular diffraction spot. This comes with the advantage of filtering out the contribution of the surface roughness in the electron reflectivity signal. However, due to misalignment of the aperture, slight intensity variations can occur. These misalignments probably cause the reduction in overall intensity and the striped artifacts in Fig. 7.6a. Filtering out of the surface roughness from the electron reflectivity data is also achieved in the diffraction data by averaging a few pixels around the maximum of the specular diffraction spot.

Finally, we investigated the surface of the $LaAlO_3/SrTiO_3/Ca_2Nb_3O_{10}$ heterostructure. Figure 7.7 shows a LEEM (a) and an AFM image (b). The nanosheets were still clearly visible. Line profiles were taken to obtain the surface roughness on top of a single flake (Fig. 7.7c). The surface roughness was less than a unit cell, pointing to an atomically flat surface.

7.4 Discussion

The first examples of perovskite growth on $Ca_2Nb_3O_{10}$ nanosheets in the literature already showed they are promising candidates for transfer of TMO devices to literally any substrate.

Here we show how low-energy electron microscopy studies can help to find the growth conditions and annealing steps required to build TMO devices on $Ca_2Nb_3O_{10}$ nanosheets. While the growth of $SrTiO_3$, $SrRuO_3$ and $BiFeO_3$ have been shown before [3], only relatively thick layers have been grown, without layer-by-layer growth control. We found that such control is not possible directly on top of

the nanosheets. A buffer layer is required to create a flat and well defined surface on the atomic scale. For $SrTiO_3$, we showed the surface changes during growth of the first 7 unit cells and this number seems to be required for the well defined surface with $SrTiO_3$-substrate-like properties. This is much more than the 1 to 2 unit cells range in which the IV-curve changes when growing $LaAlO_3$ on $SrTiO_3$.

For the first $SrTiO_3$ layer we could not obtain a crystalline film at temperatures above 660 °C and degradation of the diffraction pattern was observed before the growth started. In literature however films are grown at 700 °C[3,6]. The main difference between the conditions in Ref. 3, 6 and those reported here is the oxygen background pressure. From this we infer that nanosheets degrade in low oxygen pressures for temperatures above 660 °C. This could be caused by the reduction of oxygen in the nanosheet.

The $SrTiO_3$ film grown did not show a well-defined surface. This could be improved by annealing, which suggests that the growth temperature was too low for ideal growth. The just grown surface showed an IV-curve with many similarities to a SrO-terminated $SrTiO_3$, while after annealing at 770 °C the surface showed the IV-curve TiO_2-terminated $SrTiO_3$. This is somewhat surprising since the SrO-terminated reference curve was taken at a temperature of 770 °C, from which it can be concluded that the SrO-termination is stable at this temperature. However, the SrO-terminated reference sample was fully covered with a double layer of SrO. From this we conclude that the SrO on the grown $SrTiO_3$ is only seen on the surface due to the rough surface where it is unstable at high temperatures. Annealing reorders the surface to a well defined TiO_2-termination.

While the nanosheets were unstable at temperatures above 660 °C, no degradation is found during the annealing of the $SrTiO_3$ film on nanosheets at 770 °C. Apparently the $SrTiO_3$ layer protects the nanosheets from oxygen reduction. However, the temperature dependence is still fragile and temperatures above 770 °C are not recommended at these low pressures.

Once a well-defined surface is obtained, layer-by-layer growth of $LaAlO_3$ can be achieved. We do not find any difference between the growth of $LaAlO_3$ on our $SrTiO_3$ film on nanosheets and a TiO_2-terminated $SrTiO_3$ substrate. The final ARRES map is very similar to ARRES maps found on conducting $LaAlO_3/SrTiO_3$ heterostructures as found in chapter 6. From the comparison with the measurements performed in chapter 6, we conclude all the requirements such as surface termination en stoichiometry are in place for the $LaAlO_3/SrTiO_3$-interface to show conductivity. We however could not confirm conductivity by transport measurement because of the difficulty to contact the interface of individual flakes.

Lastly we stress the opportunity of electronic gating of TMO devices on nanosheets. We infer a minimum $SrTiO_3$ buffer layer thickness of only ≈7 unit cells. For bottom gating of devices this would mean a gate dielectric of only 7 unit cells plus the thickness of the nanosheets, which was reported to be between 1.5 and 4 nm[6–9]. This would give an upper bound of the gate dielectric of only 7 nm and provide a great possibility to improve bottom gating.

7.5 Summary

In this chapter we have shown the growth of a $LaAlO_3/SrTiO_3$ heterostructure on $Ca_2Nb_3O_{10}$ nanosheets on Si. Low-energy electron microscopy has allowed us to combine crystal information by LEED with real-space images of the nanosheets and band structure information by ARRES. The ability of in-situ PLD allows to combine this with growth analysis.

For the starting $SrTiO_3$-layer on the nanosheets, no layer-by-layer growth can be observed. The $SrTiO_3$ grown was not flat and the surface changed up to $\approx$7 unit cells as was obtained from IV-curves. A flat TiO_2-terminated $SrTiO_3$ surface could be obtained by annealing the grown $SrTiO_3$ at 770 °C. A combination of diffraction and real-space imaging showed that the $SrTiO_3$ crystal orientation depends on the underlying $Ca_2Nb_3O_{10}$ crystal structure. Between the nanosheets no crystalline $SrTiO_3$ is formed. On the flat TiO_2-terminated $SrTiO_3$ surface, layer-by-layer growth of $LaAlO_3$ could be observed.

With a combination of IV-curves and ARRES maps we could analyze the surface of the grown $LaAlO_3$ by comparing it to earlier measurements. The growth of $LaAlO_3$ showed the fingerprint of a conducting $LaAlO_3/SrTiO_3$ heterostructure found in chapter 6. Conductance however could not be measured, as this was obstructed by the difficulty to measure on as single nanosheet.

The minimum thickness of the $SrTiO_3$/nanosheet stack was determined to be around 7 nm. This implies a great opportunity to improve bottom gating of the $LaAlO_3/SrTiO_3$ interface.

References

[1] A. Ohtomo and H. Y. Hwang, *A high-mobility electron gas at the $LaAlO_3/SrTiO_3$ heterointerface*, Nature **427**, 423 (2004).

[2] J. W. Park, D. F. Bogorin, C. Cen, D. A. Felker, Y. Zhang, C. T. Nelson, C. W. Bark, C. M. Folkman, X. Q. Pan, M. S. Rzchowski, J. Levy, and C. B. Eom, *Creation of a two-dimensional electron gas at an oxide interface on silicon*, Nature Communications **1**, 94 (2010).

[3] A. P. Dral, M. Nijland, G. Koster, and J. E. ten Elshof, *Film transfer enabled by nanosheet seed layers on arbitrary sacrificial substrates*, APL Materials **3**, 056102 (2015).

[4] M. Nijland, S. Kumar, R. Lubbers, D. H. A. Blank, G. Rijnders, G. Koster, and J. E. ten Elshof, *Local Control over Nucleation of Epitaxial Thin Films by Seed Layers of Inorganic Nanosheets*, ACS Applied Materials & Interfaces **6**, 2777 (2014).

[5] T. Shibata, K. Fukuda, Y. Ebina, T. Kogure, and T. Sasaki, *One-Nanometer-Thick Seed Layer of Unilamellar Nanosheets Promotes Oriented Growth of Oxide Crystal Films*, Advanced Materials **20**, 231 (2008).

[6] H. Yuan, M. Nguyen, T. Hammer, G. Koster, G. Rijnders, and J. E. ten Elshof, *Synthesis of $KCa_2Nb_3O_{10}$ Crystals with Varying Grain Sizes and Their Nanosheet Monolayer Films As Seed Layers for PiezoMEMS Applications*, ACS Applied Materials & Interfaces **7**, 27473 (2015).

[7] H. Tetsuka, H. Takashima, K. Ikegami, H. Nanjo, T. Ebina, and F. Mizukami, *Nanosheet Seed-Layer Assists Oriented Growth of Highly Luminescent Perovskite Films*, Chemistry of Materials **21**, 21 (2009).

[8] M. Osada, K. Akatsuka, Y. Ebina, H. Funakubo, K. Ono, K. Takada, and T. Sasaki, *Robust High-nkappa Response in Molecularly Thin Perovskite Nanosheets*, ACS Nano **4**, 5225 (2010).

[9] K. Akatsuka, G. Takanashi, Y. Ebina, M.-a. Haga, and T. Sasaki, *Electronic Band Structure of Exfoliated Titanium- and/or Niobium-Based Oxide Nanosheets Probed by Electrochemical and Photoelectrochemical Measurements*, The Journal of Physical Chemistry C **116**, 12426 (2012).

[10] S. M. Schramm, J. Kautz, A. Berghaus, O. Schaff, R. M. Tromp, and S. J. van der Molen, *Low-energy electron microscopy and spectroscopy with ESCHER: Status and prospects*, IBM Journal of Research and Development **55**, 1:1 (2011).

[11] R. Tromp, J. Hannon, A. Ellis, W. Wan, A. Berghaus, and O. Schaff, *A new aberration-corrected, energy-filtered LEEM/PEEM instrument. I. Principles and design*, Ultramicroscopy **110**, 852 (2010).

[12] S. M. Schramm, A. B. Pang, M. S. Altman, and R. M. Tromp, *A Contrast Transfer Function approach for image calculations in standard and aberration-corrected LEEM and PEEM*, Ultramicroscopy **115**, 88 (2012).

[13] R. Tromp, J. Hannon, W. Wan, A. Berghaus, and O. Schaff, *A new aberration-corrected, energy-filtered LEEM/PEEM instrument II. Operation and results*, Ultramicroscopy (2013).

[14] M. Kawasaki, K. Takahashi, T. Maeda, R. Tsuchiya, M. Shinohara, O. Ishiyama, T. Yonezawa, M. Yoshimoto, and H. Koinuma, *Atomic Control of the $SrTiO_3$ Crystal Surface*, Science **266**, 1540 (1994).

[15] J. B. Hannon, J. Sun, K. Pohl, and G. L. Kellogg, *Origins of Nanoscale Heterogeneity in Ultrathin Films*, Physical Review Letters **96**, 246103 (2006).

[16] J. Jobst, J. Kautz, D. Geelen, R. M. Tromp, and S. J. van der Molen, *Nanoscale measurements of unoccupied band dispersion in few-layer graphene*, Nature Communications **6**, 8926 (2015).

[17] M. Horn-von Hoegen, *Growth of semiconductor layers studied by spot profile analysing low energy electron diffraction Part I1*, Zeitschrift fr Kristallographie - Crystalline Materials **214**, 591 (1999).